Contents

Part 1

Experimental setup: Collider, detector and algorithms

1.1 The Large Hadron Collider

The Large Hadron Collider (LHC) [1, 2] is a particle accelerator installed in the former LEP [3] tunnel at CERN [4]. It is 26.7 km in circumference and consists of two separate rings, which are, in periods of operation, inhabited by two counter-circulating beams. At the interaction points of the two beams, either proton-proton collisions or heavy ion collisions take place. In this thesis, only *pp*-collision data from the year 2012 is analysed. Thus, all machine values cited in the following chapters and paragraphs refer to the setup for *pp*-collisions in 2012 if not stated otherwise.

The beams are separated into bunches which rotate with a bunch spacing of 50 ns corresponding to a collision frequency of 20 MHz. Before the bunches are actually filled into the LHC ring they are pre-accelerated in other accelerators, which are in the order they are actually passed by the protons: Linac2, Proton Synchrotron Booster (PSB), Proton Synchrotron (PS), Super Proton Synchrotron (SPS). The injector chain and the LHC ring with its experiments is visualised in Fig 1.1.

In the LHC, the beams are kept on their circular path with the help of a magnetic field of
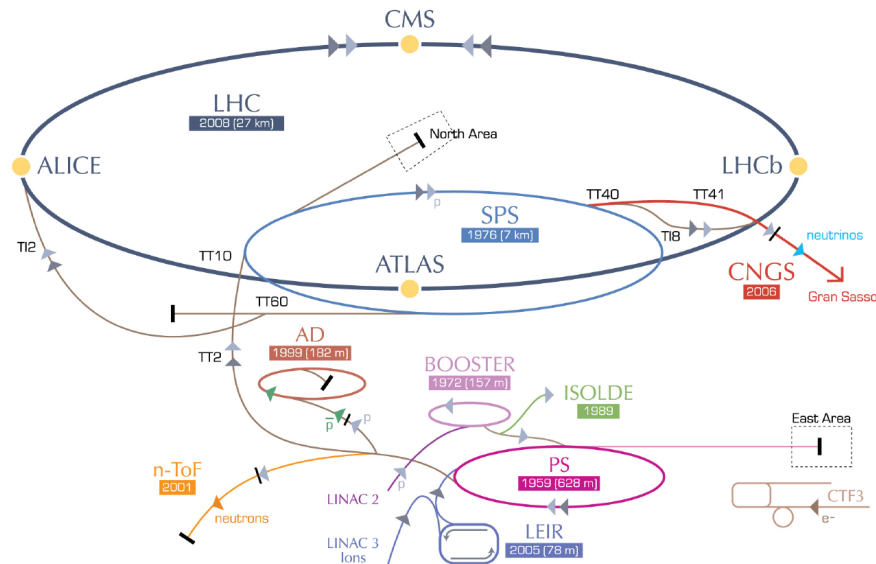

Figure 1.1: Visualisation of the LHC with its experiments and the injector chain. Taken from [5].

4.76 T. Further quadrupole and sextupole magnets squeeze and focus the bunches resulting in a bunch spread of roughly 8 cm length and a Gaussian shape radius of 20 μm RMS at the interaction point. The number of protons contained in each bunch is of the order 10^{11}. The LHC hosts four main particle physics experiments: the CMS, ATLAS, LHCb and ALICE experiments. CMS [6, 7] and ATLAS [8–10] are so-called "general purpose experiments", that are used for a variety of different physics analyses. In contrast, the LHCb [11] and ALICE [12] experiments are designed with an emphasis on CP-violation measurements and heavy ion collisions, respectively. Each experiment is thus interested in different processes that happen at the beam collision points.

The number of expected events for a given process can be expressed in terms of the corresponding cross section σ times the integrated luminosity

$$N = L \cdot \sigma, \tag{1.1}$$

with an integrated luminosity of $L = \int \mathcal{L} \, dt$, where $\mathcal{L}$ is the instantaneous luminosity. The instantaneous luminosity $\mathcal{L}$ depends on several machine parameters, such as the collision frequency f, the number of particles in the bunches n_1 and n_2, the spread in the transverse plane of the bunches σ_x and σ_y, and a geometrical correction parameter F due to the crossing angle of the two bunches at the interaction point:

$$\mathcal{L} = \frac{f n_1 n_2}{4\pi \sigma_x \sigma_y} \cdot F. \tag{1.2}$$

In 2012, the peak luminosity was $7.7 \cdot 10^{33} \frac{1}{\text{cm}^2 \text{s}}$. The total integrated luminosity of *pp*-collisions over time recorded at the CMS experiment is shown in Fig. 1.2.
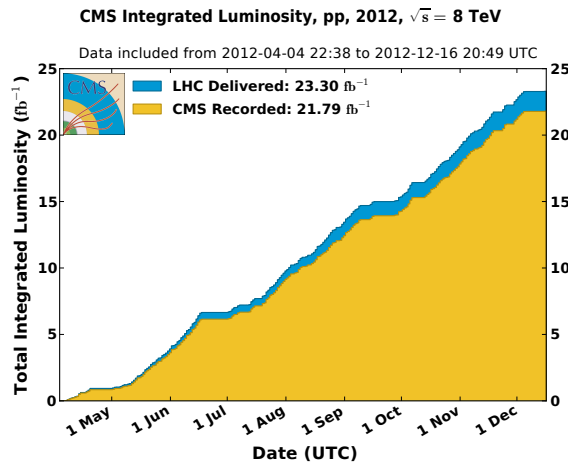

Figure 1.2: Integrated luminosity delivered by LHC (blue) and recorded by CMS (orange) in the year 2012. Taken from [13].

1.2 The CMS detector

The Compact Muon Solenoid (CMS) detector [6,7] is a general purpose detector, designed to explore particle physics phenomena up to the multi-TeV scale. The detector concept is an onion-like structure of different layers, each one made up of a different type of detector. The CMS detector measures $21.6\,\text{m}$ in length and $14.6\,\text{m}$ in diameter with a total weight of $12\,500\,\text{tons}$. In Fig. 1.3, a perspective view of the CMS detector is depicted.

The coordinate system used at CMS consists of the pseudorapidity $\eta = -\ln\tan\frac{\theta}{2}$ and the azimuthal angle ϕ. The advantage of the pseudorapidity η is the Lorentz invariance with respect to the z-axis (beam axis). The angle ϕ covers the direction in the $x-y$ plane (orthogonal to the beam axis).

In order to measure the momentum of charged particles a superconducting solenoid is incorporated between the calorimeter system and the muon system providing a uniform axial magnet field of $3.8\,\text{T}$. Iron yokes contained within the muon system ensure the return of the magnetic flux.
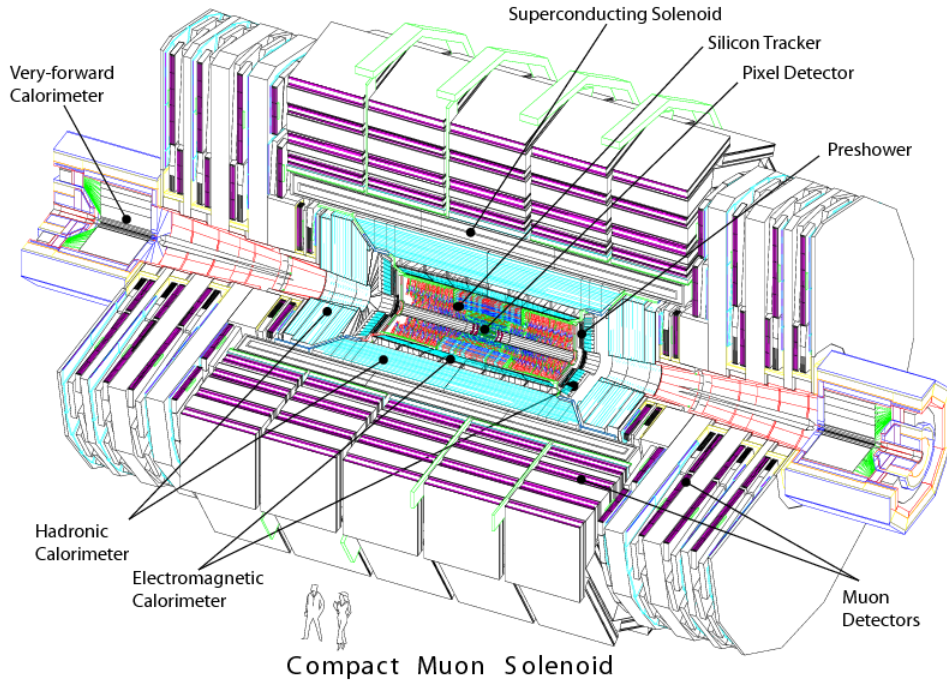

Figure 1.3: A perspective view of the CMS detector. Taken from [6]

71   In the following, the various detector components of the CMS detector from the inside
72 to the outside as well as the trigger system will be explained.

1.2.1 The tracking system

74 The tracking detector [14–16] is the innermost detector at CMS. It is a silicon semicon-
75 ductor detector and is included for the tasks of vertex and track reconstruction by the
76 measurement of particles' energy losses. A schematic sketch of the tracker at CMS is de-
77 picted in Fig. 1.4. The tracking system is divided into two parts: the innermost tracker is
78 a silicon pixel detector surrounded by a silicon strip detector. Both parts will be explained
79 in detail in the upcoming sections, followed by a short description of how the energy of
80 a traversing particle is measured with the silicon sensors. As a calibration of the silicon
81 pixel detector was performed within this PhD thesis (see Section ??), an emphasis will be
82 put on the pixel detector.

The silicon pixel tracker

84 The silicon pixel detector consists of three different cylindrical layers in the barrel region at
85 radii of 4.4 cm, 7.3 cm and 10.2 cm and two discs in the endcaps at z-distances of 34.5 cm
86 and 46.5 cm. It is made up of 1440 modules in total (barrel + endcaps), each module
87 comprising 8 or 16 read-out-chips (ROCs). The read-out-chips are bump bonded [18] to a
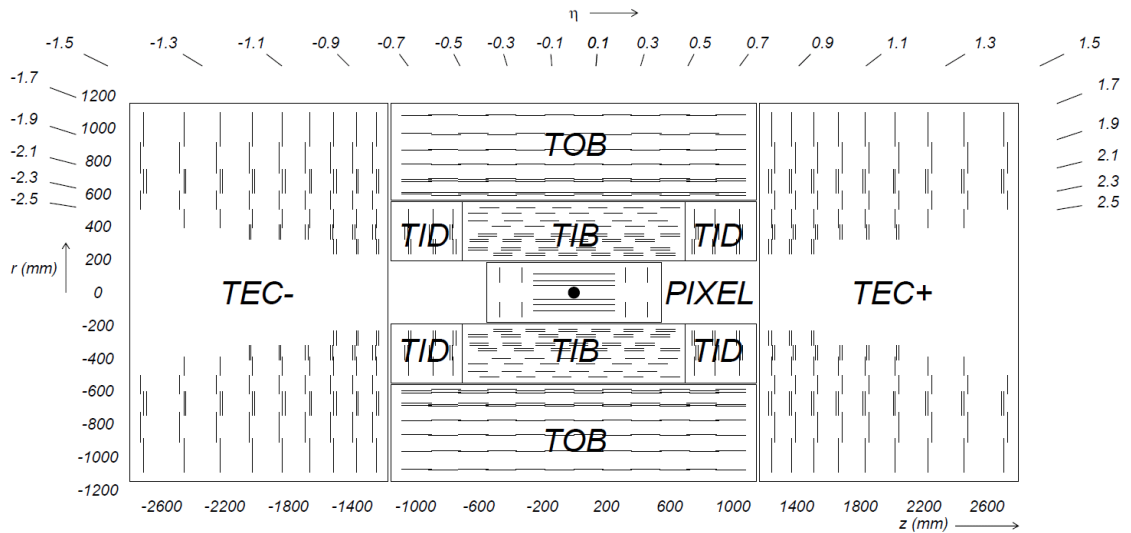

Figure 1.4: Schematic sketch of the silicon tracker at CMS in the $z - \phi$ plane including
the silicon pixel detector (PIXEL) as well as the different components of the
silicon strip detector: tracker inner barrel (TIB), tracker outer barrel (TOB),
tracker endcap (TEC), and tracker inner disk (TID). Taken from [17].

88 pixel system of 52×80 pixels, which are read out in double columns (see [18] on detailed
89 information of the readout electronics). A visualisation of a part of a pixel module is
90 shown in Fig. 1.5. In total, there are 65 million pixels comprised in the pixel detector.
91 The large number of pixels and their small size ensure a low occupancy close to the vertex
92 of around $0.002 - 0.02\%$ [17] and a high hit efficiency of around 99% [19].

93   The silicon pixel detector is very important for the reconstruction of primary and sec-
94 ondary vertices as well as the reconstruction of particle tracks. Therefore, a high spatial
95 resolution is needed. This is achieved by the small size of the pixels $(150 \times 100 \, \mu\text{m}^2)$ and
96 the exploitation of the spread of the energy deposition across several pixels (in average
97 the energy is deposited across 3-5 pixels [20]). Exploiting the energy spread across pixels,
98 a spatial resolution in the barrel region of $9.4 \, \mu\text{m}$ in the $r - \phi$ plane and - dependent on
99 the incident angle of a track - a hit resolution between $20 - 45 \, \mu\text{m}$ in the z-direction is
100 achieved [17]. The spatial resolution of the primary vertex depends on the number of
101 tracks taken into account for the reconstruction of the primary vertex. For more than 50
102 tracks originating from the primary vertex the spatial resolution is around $10 - 12 \, \mu\text{m}$ for
103 each of the three spatial dimensions [17]. The reconstruction efficiency of primary vertices
104 is close to 100% if more than two tracks are used for the vertex reconstruction [17].
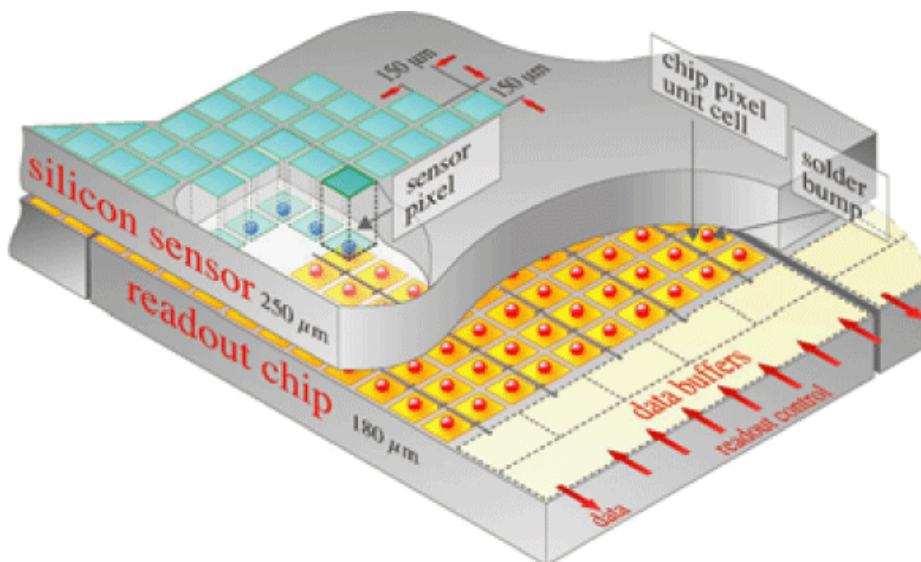

Figure 1.5: Schematic sketch of a part of a silicon pixel tracker module including the silicon
sensors and the read-out-chip (ROC). Taken from [17].

The silicon strip tracker

The silicon strip tracker is the next-to innermost detector of the CMS detector and ranges up to a radius of $1.1\,\mathrm{m}$. The barrel region consists of a tracker inner barrel (TIB) and a tracker outer barrel (TOB). The TIB has four layers with two layers equipped with stereo modules to measure the hit position additionally in the $r - z$ plane. The silicon sensors in the TIB are of $320\,\mu\mathrm{m}$ thickness with a strip pitch varying between $80 - 120\,\mu\mathrm{m}$. The TOB has six different layers (two layers of stereo modules) with silicon sensors of $500\,\mu\mathrm{m}$ thickness and strip pitches between 120 and $180\,\mu\mathrm{m}$.

The endcaps are subdivided into a tracker endcap (TEC) and a tracker inner disk (TID). They ensure a coverage of a pseudorapidity up to $|\eta| = 2.5$. In each TEC, 9 disks between a z-position of $120\,\mathrm{cm} < z < 280\,\mathrm{cm}$ are contained. Each of the TID comprises three disks between $60\,\mathrm{cm} < z < 110\,\mathrm{cm}$.

In the barrel region, a single-point resolution between $23 - 52\,\mu\mathrm{m}$ in the $r - \phi$ plane and $230 - 530\,\mu\mathrm{m}$ in the z-direction is achieved.

Energy measurements in the tracking system

A charged particle traversing the above mentioned silicon detectors produces electron-hole pairs in the semiconducting material along its trajectory, thus loosing energy due to ionisation. For silicon, the mean energy to create an electron-hole pair is $3.61\,\mathrm{eV}$ at $-10°\mathrm{C}$. Minimally ionising particles produce an average of $22\,000$ electron-hole pairs in silicon sensors [18]. Electrons that are subject to a hard collision with the incoming particle (so-called delta-rays), produce further ionisation and can thus lead to much higher energy deposits in the silicon. Because of the applied bias voltage at the sensors (for the creation of a depletion zone), the released electrons (holes) travel to the n-contacts (p-contacts), thereby inducing a current which is measured by the readout electronics. A more detailed description of the energy measurement in silicon sensors can be found in [18].

1.2.2 The electromagnetic calorimeter

The electromagnetic calorimeter (ECAL) [14, 21] encloses the tracking system and starts at a radius of $129\,\mathrm{cm}$ in the barrel region. It is divided into a barrel part and two endcaps, which are at a distance of $314\,\mathrm{cm}$ from the vertex. Figure 1.6 depicts a schematic sketch of the electromagnetic calorimeter system in the transverse plane. It can be seen, that the ECAL barrel (EB) covers a pseudorapidity region up to $|\eta| = 1.479$. The ECAL endcaps (EE) start at $|\eta| = 1.653$ and reach up to $|\eta| = 3.0$. Before the endcaps, a preshower detector ($1.653 < |\eta| < 2.6$) is installed with the main task to identify neutral pions in the endcaps. It additionally improves the position measurement of electrons and photons.
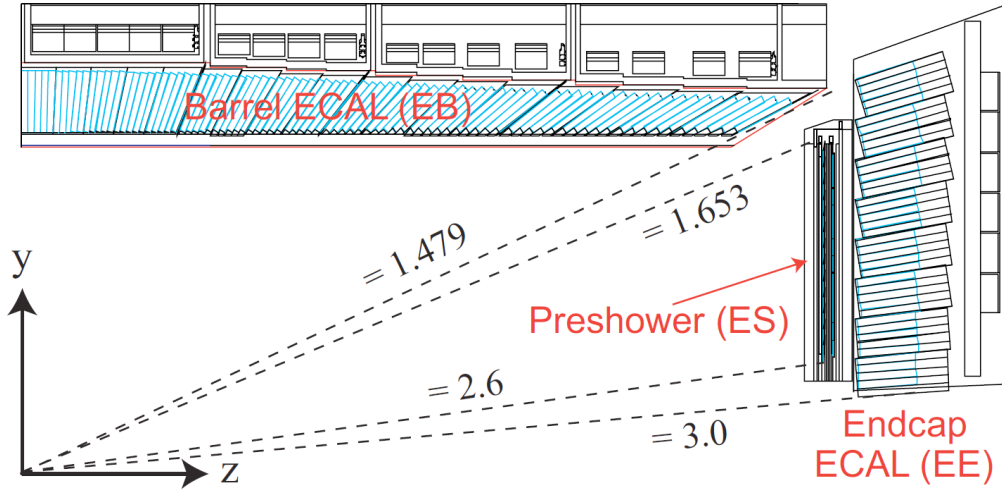
Figure 1.6: A quarter section of the ECAL in a transverse view. Taken from [14].

The EB and EE consist of lead tungstate (PbWO$_4$) scintillating crystals, 61200 in the barrel region and 7324 in the endcaps. Their advantage is the short radiation length (X$_0$=0.89 cm) and a small Molière radius (2.2 cm). Thus, particles deposit their energy on rather short distances and a compact design is possible. To detect the rather low light yield (30γ/ MeV) of a traversing particle, silicon avalanche photodiodes (APDs) are used in the barrel region and vacuum phototriodes (VPTs) in the endcaps. For information on the readout electronics, the reader is referred to [14].

The resolution of an energy measurement in the calorimeter can be expressed by

$$\left(\frac{\sigma}{E}\right)^2 = \left(\frac{S}{\sqrt{E}}\right)^2 + \left(\frac{N}{E}\right)^2 + C^2, \tag{1.3}$$

with S referring to the stochastic term, N to the noise term, and C to a constant term. For the ECAL the parameters of Eq. (1.3) are measured to $S = 3.63\sqrt{\text{GeV}}$, $N = 0.124\,\text{GeV}$, and $C = 0.26$ [14]. These numbers lead to an energy resolution of around 0.4% for an electron with $E \approx 200\,\text{GeV}$ and around 0.6% for an electron with $E \approx 50\,\text{GeV}$.

1.2.3 The hadronic calorimeter

The hadronic calorimeter (HCAL) [14,22] of the CMS detector is splitted into four different detector modules: the hadron barrel (HB), the hadron outer (HO), the hadron endcap (HE) and the hadron forward (HF) calorimeters. A schematic sketch is depicted in Fig. 1.7.

The HCAL is dedicated to measuring the energy of hadrons as well as providing a good estimate of the missing energy in the event. The latter one is achieved by the
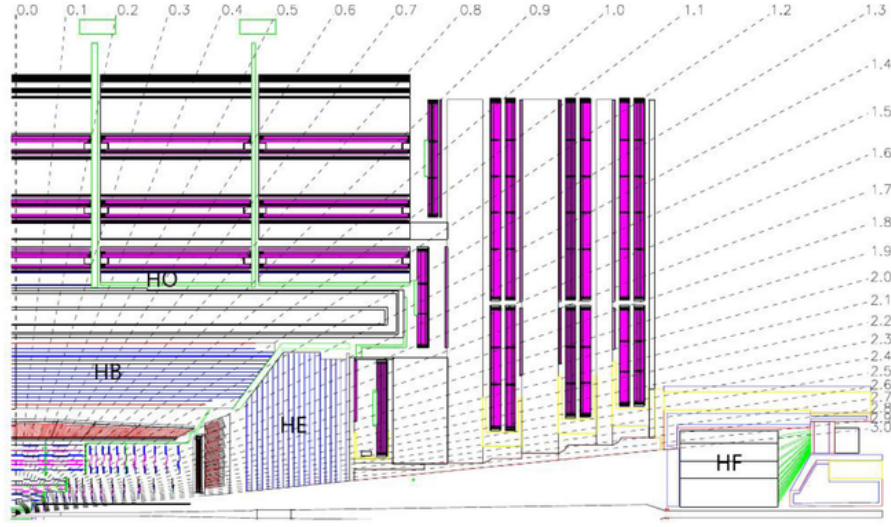
Figure 1.7: A quarter section of the HCAL in a transverse view. Taken from [23].

high pseudorapidity coverage ($|\eta| < 5.0$) that assures the detection of most of the visible particles.

The HCAL is a so-called sampling calorimeter which consists of brass absorber material, initiating the hadronic shower, as well as active plastic scintillators. The emitted photons are read out with wavelength-shifting (WLS) fibres which are embedded into the scintillators. These in turn are connected to clear fibres that transfer the light to the readout system.

The hadron barrel (HB) covers the pseudorapidity range between $-1.4 < \eta < 1.4$. It is composed of 17 layers of absorber material (15 brass and 2 steel layers) interleaved with scintillator layers. The scintillator layers are divided into 2304 towers with a size of $\Delta\eta \times \Delta\phi = 0.087 \times 0.087$.

The hadron outer (HO) covers a pseudorapidity range up to $|\eta| = 1.26$ and is divided into sectors which match the ϕ segmentation of the drift-tube chambers of the muon system (see Section 1.2.4). It is located between the solenoid and the barrel detector of the muon system. The HO is dedicated to measuring the energy of the shower leakage of hadrons. Its thickness corresponds to over ten interaction lengths.

The hadron endcap (HE) extends the pseudorapidity coverage of the HCAL up to $|\eta| = 3.0$ and starts at $|\eta| = 1.3$. It consists of 2304 towers in total, which vary in size between $5 - 10°$ in the ϕ direction and $0.087 - 0.35$ in η direction.

Finally, the hadron forward (HF) calorimeter extends the pseudorapidity range up to $|\eta| = 5.0$, starting from $|\eta| = 3.0$. It is build out of steel plates, which contain $1\,\mathrm{mm}^2$ grooves containing quartz fibres. The emitted light by the quartz fibres is transferred to photomultipliers. The HF is divided into 13 towers where almost all towers have a spread

182 of $\Delta\eta \approx 0.175$ in η direction and $\sim 10°$ in ϕ direction.

1.2.4 The muon system

184 The muon system [14,24] is the outermost detector component at CMS. It comprises three
185 different types of gaseous detectors, mounted into the iron return yokes: drift tube (DT)
186 chambers in the barrel region ($|\eta| < 1.2$), cathode strip chambers (CSC) in the endcap
187 region ($1.04 < |\eta| < 2.4$) and resistive plate chambers (RPC) in the barrel as well as the
188 endcap region ($|\eta| < 1.6$) (see Fig. 1.8 for a schematic sketch of the muon system). In
189 the barrel part of the muon system, four layers (so-called stations) of drift-tube chambers
190 are assembled inside the iron return yoke layers at radii of 4.0, 4.9, 5.9 and 7.0 m from
191 the beam axis. The position of a muon traversing these layers can be measured with a
192 precision of $\approx 100\,\mu$m in radial direction and $\approx 1\,$mrad in ϕ direction.

193 The four endcap disks are made up of 468 cathode strip chambers in total. By measuring
194 the centre-of-gravity, they achieve a spatial resolution of $\approx 100 - 200\,\mu$m and an angular
195 resolution of $\approx 10\,$mrad in ϕ direction. They are designed in order to cope with a high
196 particle flux of about 1kHz/cm^2 and a non-uniform magnetic field. As signals can be
197 transferred very fast, they are used for the level-1 trigger system.

198 Finally, the resistive plate chambers cover the barrel as well as the endcap region up to
199 a pseudorapidity of $\eta = 1.6$. They provide a fast response with a good time resolution
200 enabling the exact identification of the respective bunch-crossing. It is used for the level-1
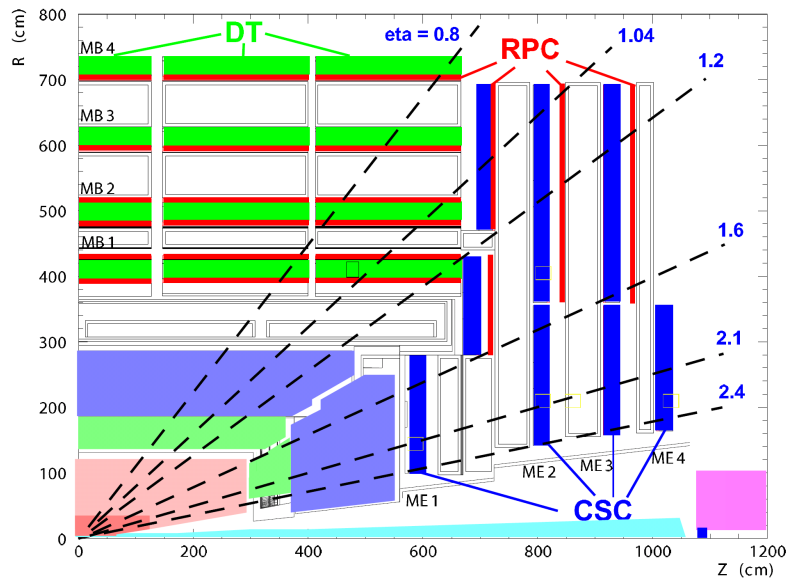

Figure 1.8: A quarter section of the CMS detector in the transverse plane with a detailed view on the muon system. Taken from [14].

trigger system as well.

1.2.5 The trigger system

Because of the impossibility of storing each event occurring at the CMS experiment, a multistage trigger system [14] is used to achieve a drastic reduction of recorded events by nearly six orders of magnitude. It comprises two main parts: a so-called level-1 (L1) trigger system and a high-level trigger (HLT) system.

The L1 triggers need to provide a very fast decision ($3.2 \, \mu$s, where around $1 \, \mu$s is allocated to the actual L1 trigger calculations) whether an event shall be recorded or not. During this time, the recorded event data is held in buffers located close to the single detector components. Information from the muon system and the calorimeters is used for the L1-trigger decisions. Objects used for these decisions are so-called "trigger primitive" objects: photons, electrons, muons, jets above certain E_T and p_T thresholds and global variables like missing transverse energy, $\not{E}_\mathrm{T}$. The design value of the number of events per second that pass this trigger stage is $100 \, \mathrm{kHz}$.

After a time of $3.2 \, \mu$s, the stored data in the buffers close to the single detector components are transferred to the front-end readout buffers in case the event passed the L1-trigger requirements. By partial event reconstruction and the use of various trigger levels (calorimeter, muon information followed by pixel information and full event reconstruction), higher event objects can be used to check whether HLT-trigger requirements are fulfilled. On HLT level, the decision time amounts to $50 \, \mathrm{ms}$ and a reduction from $100 \, \mathrm{kHz}$ to $100 \, \mathrm{Hz}$ of event recording is achieved.

1.3 Event reconstruction and particle identification

A crucial ingredient of data analysis at the CMS experiment, is the translation of the energy measurements in the various sub-detector components into physical objects, like muons, electrons, etc. . For this translation, i.e. particle identification, information from all detector components are used. This is known as the particle-flow event reconstruction algorithm [25]. In Fig. 1.9, a slice through the CMS detector is shown with the signatures of different particles indicated as coloured lines.

In the next section an introduction into this algorithm is given, followed by the definition and classification of physics objects at the CMS experiment.
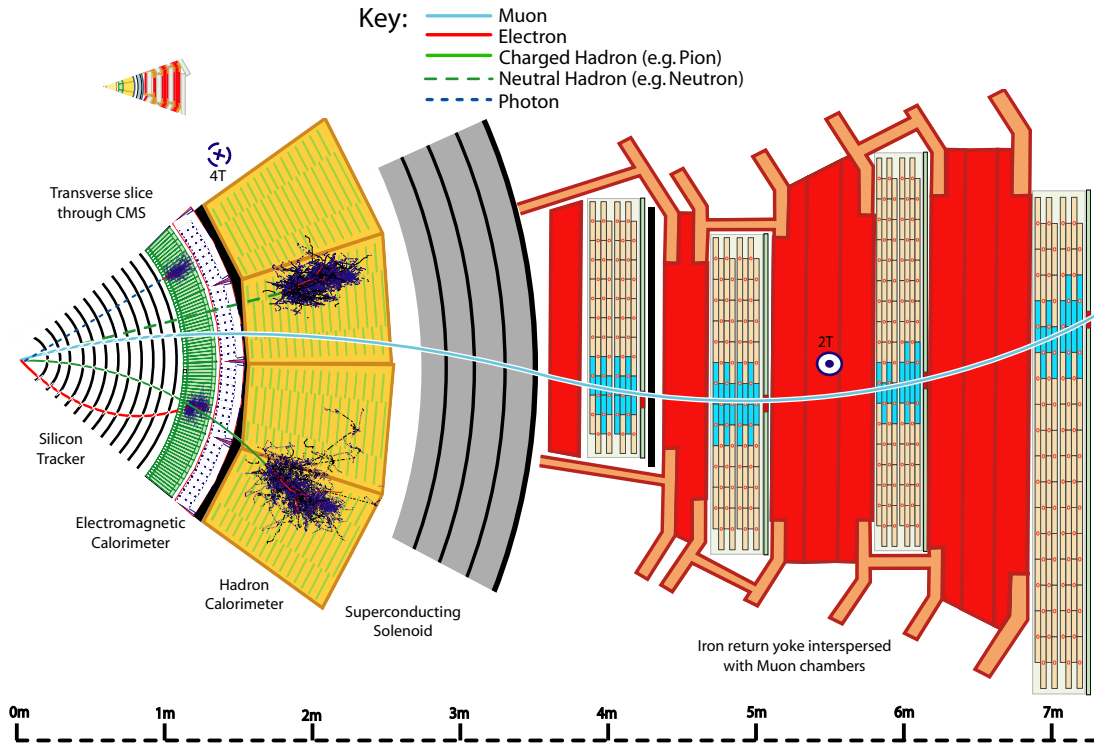
Figure 1.9: A radial slice through the CMS detector with several particle signatures indicated as coloured lines. Taken from [26].

1.3.1 The particle-flow algorithm

The particle-flow (PF) event description [25] aims at optimising particle identification by the usage of all sub-detector components of the CMS detector. There are three main building bricks used for the global event description: reconstructed charged-particle tracks, calorimeter clusters, and muon tracks. The main requirements for these building bricks is a high reconstruction efficiency as well as a small fake rate. Therefore, a special emphasis was put on developing a very efficient tracking algorithm (see Section 1.3.2) and a well performing calorimeter clustering algorithm [25].

The particle-flow algorithm proceeds as follows in an event (the description is based on [25]):

1. For each pair of detected building bricks, a distance in the $\eta - \phi$ plane is calculated in order to quantify the quality of their link (whether the two building bricks stem from the same particle).

2. "Blocks" are produced from the building bricks that are linked together (with a typical number of one, two or three building bricks contained in a block).

3. For each block the following steps are performed:

    a) Each global muon (hits detected in the tracker as well as in the muon system) where the p_T measured in both sub-detectors is compatible with the tracker measurement only is defined as particle-flow muon and the track in both sub-detectors is removed from the block.

    b) Electron reconstruction and identification follows using tracker hits and ECAL clusters. For an identified particle-flow electron, the corresponding tracker hits and the ECAL clusters (including energy deposits from Bremsstrahlung photons) are removed from the block.

    c) Tighter tracker quality criteria are applied.

    d) The compatibility of the remaining ECAL and HCAL energy deposits to the transverse momentum of the reconstructed tracks within a block is checked. This allows for the identification of particle-flow charged hadrons with a momentum estimate using tracker and calorimeter information. Only, if the energy deposits in the ECAL or HCAL are much larger than the corresponding track p_T, it gives rise to a particle-flow photon or particle-flow neutral hadron, respectively. All used ECAL and HCAL clusters used for the identification as well as the reconstructed tracks are removed from the block.

    e) Finally, the remaining HCAL and ECAL clusters (which are all not linked to any other building block) give rise to particle-flow photons or particle-flow neutral hadrons.

These identified particle-flow objects are used to identify further objects in the event, e. g. the missing transverse-energy or decay products of a tau lepton.

1.3.2 Object reconstruction

In this section, an overview about the required criteria for the identification of particles and other physics object is given.

1.3.2.1 Reconstruction of tracks

The reconstruction of tracks aims at linking several hits in the tracking system to one reconstructed track that matches with a high probability the original trajectory of the particle. With the track reconstruction an estimate of the particle's momentum as well as the position can be achieved. The challenge arise due to the high combinatorial complexity because of the large number of hits detected in each event, especially in the layers close to the interaction vertex. In the following, an overview about the tracking algorithm

used at CMS is given. It is based on [17] and the reader is referred to this reference for a thorough description of the reconstruction of tracks at CMS.

The developed tracking software used at CMS is usually referred to as the Combinatorial Track Finder (CTF). It grounds on the so-called combinatorial Kalman filter [27–29] (which in turn is based on the Kalman filter [30]), which is mathematically equivalent to a global least square minimisation for linear models with Gaussian noise.

The basic idea of the tracking algorithm at CMS is to not apply the combinatorial Kalman filter on all hits in one step but to reduce the level of complexity by an iterative procedure (called iterative tracking). A reduction of complexity can be achieved by reconstructing tracks in the first step that are easy to identify because of e.g. a high p_T. These tracks are removed afterwards and the remaining tracker hits are subject to further reconstruction iterations. The following iterations are performed:

- Iteration 0: Tracks near to the *pp*-interaction point that have three pixel hits and a $p_\mathrm{T} > 0.8\,\mathrm{GeV}$ are reconstructed.

- Iteration 1: Tracks with only two pixel hits and $p_\mathrm{T} > 0.8\,\mathrm{GeV}$ are recovered.

- Iteration 2: Low p_T tracks from the *pp*-interaction point are reconstructed.

- Iteration 3-5: Reconstruction of tracks that are not originating from the primary vertex and recovering of tracks not found by previous iterations.

Within these iterations, the reconstruction is subdivided into four different steps:

- Seed generation: Only 2-3 hits are used to define track candidates.

- Extrapolation: Based on expected flight path, additional hits are assigned to the candidate track (use of Kalman filter).

- Parameter estimates: With the usage of the Kalman filter and a smoother, the trajectory parameters are determined.

- Setting of quality flags: Quality flags are assigned to all tracks and tracks that fail certain quality criteria are discarded.

The configuration of the first and the fourth step differ across the different iterations.

A special task when reconstruction tracks consists in the suppression of fake tracks, i.e. tracks that are not associated with a charged particle. Therefore, the requirement of fulfilling certain quality criteria (fourth step) is crucial to substantially reduce the contamination of fake tracks. For this purposes, requirements on the following variables are imposed:

312   • A minimum number of layers in which the track has an associated hit.

313   • A minimum number of layers in which the track has an associated 3-D hit.

314   • A maximum number of layers in which the track has no associated hit.

315   • $\chi^2/\mathrm{ndof} < \alpha_0 N_{layers}$.

316   • $|d_0^{\mathrm{BS}}|/\delta d_0 < (\alpha_3 N_{layers})^{\beta}$.

317   • $|z_0^{\mathrm{PV}}|/\delta z_0 < (\alpha_4 N_{layers})^{\beta}$.

318   • $|d_0^{\mathrm{BS}}|/\sigma_{d_0}(p_{\mathrm{T}}) < (\alpha_1 N_{layers})^{\beta}$.

319   • $|z_0^{\mathrm{PV}}|/\sigma_{z_0}(p_{\mathrm{T}}, \eta) < (\alpha_2 N_{layers})^{\beta}$.

320 The variable d_0^{BS} is the distance of the track to the centre of the beam-spot in the transverse
321 plane to the beam-line and z_0^{PV} is the distance along the beam-line to the closest pixel.
322 The variables δd_0 and δz_0 are the uncertainties on the distance (impact) parameters and
323 σ is the standard deviation corresponding to the length of the beam-spot in z-direction.
324 The parameters α and β have in general different values in the various iterations.

1.3.2.2 Reconstruction of jets

326 In Section 1.3.1, the reconstruction of particle-flow neutral and charged hadrons was al-
327 ready introduced. Charged and neutral hadrons are usually formed due to the hadro-
328 nisation process of final state quarks and gluons. Since the interest at particle colliders
329 concerns the sum of all particles arising from one final state gluon or quark, which is
330 referred to as a jet, the reconstruction of jets is a very important task at particle colliders.
331 Foremost, the clustering of the particle-flow candidates to a jet is a crucial ingredient for
332 the reconstruction of jets. Furthermore, the calibration of the measured jet transverse
333 momentum as well as the subtraction of energy due to pileup interactions is important to
334 ensure a good quality p_{T} measurement of jets at CMS. All three subjects are explained in
335 detail in the following sections.

Clustering of jets

337 As already noted, jets are formed by quarks or gluons in the final state that hadronise
338 due to colour confinement. The reconstruction of jets is therefore subject to a clustering
339 algorithm that clusters reconstructed particle-flow objects into a jet. At CMS, the so-
340 called anti-k_{T} cluster algorithm [31] is used. This cluster algorithm belongs to the class
341 of sequential recombination jet algorithms.

In sequential recombination algorithms, a distance measure between two particles - or more generally objects - is used to cluster them into jet cones. For this purposes, two quantities are defined

$$d_{ij} = \min \left(p_{\mathrm{T},i}^{2k}, p_{\mathrm{T},j}^{2k} \right) \frac{\Delta_{ij}^2}{R^2},$$
$$d_{iB} = p_{\mathrm{T},i}^{2k},$$

(1.4)

with Δ_{ij} referring to the distance between particles i and j in the $\eta - \phi$ plane and R denoting the radius parameter of the algorithm which determines the cluster scale. The quantity k can be any integer and specifies the behaviour of the algorithm, as will be seen later. The algorithm is an iterative procedure comprising the following steps: First, the quantities d_{iB} and d_{ij} are calculated for every single and every pair of "objects" in the event, respectively. An object can be a particle or a set of already clustered particles. If the smallest quantity is a distance between a pair of objects, these objects are clustered together. If the smallest quantity is d_{iB}, the corresponding object is considered a jet and removed from the object list. If all objects are removed from the input list of the algorithm, the clustering comes to an end.

As noted before, the integer k in Eq. (1.4) defines different types of algorithms. For the choice of $k = 0$, the algorithm is referred to as Cambridge/Aachen algorithm [32, 33]. It doesn't take the momentum of particles into account for the clustering but is only based on spatial information. The k_{T} algorithm [34, 35] exploits the configuration with $k = 1$, and starts the clustering therefore with low momentum particles. At CMS, the anti-k_{T} algorithm is used with $k = -1$. It begins with clustering high momentum particles and thus lead to very regular shapes of the jet cones. The behaviour of the three different clustering algorithm is illustrated in Fig. 1.10. One single parton-level event was subject to the three different jet clustering algorithms. Roughly 1000 soft particles are added to the event in order to test the adaptiveness of the jet algorithms to soft particles. It can be seen, that the Cambridge/Aachen and the k_{T} algorithm are both much more influenced by the addition of soft particles than the anti-k_{T} method.

Throughout this thesis jets clustered with the anti-k_{T} algorithm with a radius parameter of $R = 0.5$ are used.

Jet energy calibration

In order to account for possible mismeasurements of the jet transverse momentum, all jets at CMS are subject to a calibration procedure. This calibration aims at eliminating discrepancies between the measured jet p_{T} and the true jet p_{T} because of pileup interactions (level-1 corrections) as well as discrepancies depending on jet p_{T} and η (level-2 and level-3 corrections). Finally, in order to get rid of differences between data and simulation, jets measured in data are additional calibrated by residual correction factors (level-2 and
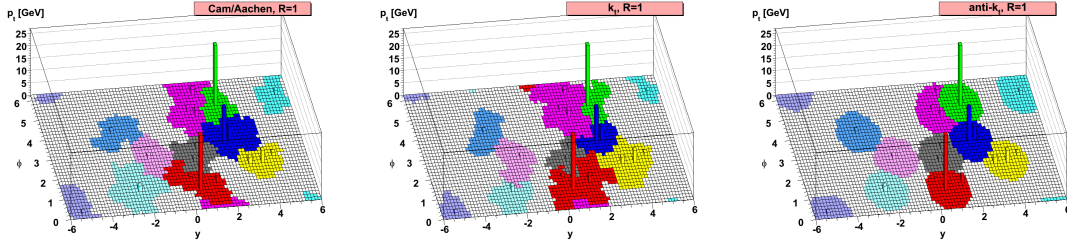
Figure 1.10: Parton-level event with ~ 1000 soft particles added. Three different algorithms are used to cluster the particles into jet cones: the Cambridge/Aachen algorithm (left), the k_T algorithm (middle), and the anti-k_T algorithm (right).

level-3 residual corrections). An overview of the applied correction factors on the measured jet p_T in simulation and data is shown in Fig. 1.11.

In the following, a more detailed description of the determination of the factorised calibration factors will be given. For a extensive description of the calibration approach, the reader is referred to [37]

L1 pileup offset corrections: In order to eliminate a mismeasurement of the jet p_T because of pileup interactions, correction factors are determined that are suppose to restore the true jet p_T. This correction is determined in bins of jet p_T, jet η, the effective jet area A, and the event energy density ρ. The correction factors are determined with a simulated QCD-multijet sample and are applied to measured data as well as simulated events.

L2 relative + L3 absolute corrections: These two corrections are devoted to correct the measured jet p_T in order to ensure a uniform response vs. η (L2) and p_T (L3).
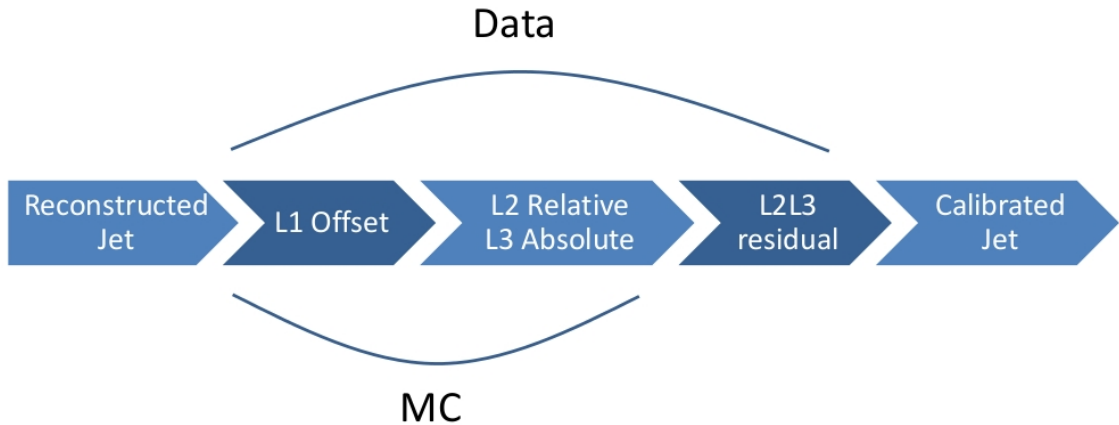

Figure 1.11: Visualisation of the various steps of the jet energy calibration at the CMS experiment. Taken from [36].

389 They are also determined on a simulated QCD-multijet sample and applied on sim-
390 ulation and data.

391 **L2L3 residual corrections:** Finally, correction factors aer determined which are ap-
392 plied on data. They ensure the elimination of differences between simulation and
393 data. They are estimated with the help of QCD-multijet events to eliminate differ-
394 ences in η (L2) and with $\gamma/Z+$ jets events in order to eliminate differences in p_T (L3).

395

396 The derived correction factors are applied on the measured transverse momentum in a
397 factorised approach according to the following equation:

$$p_\mathrm{T}^\mathrm{cor} = C_\mathrm{offset}(p_\mathrm{T}^\mathrm{raw}, \eta) \cdot C_\mathrm{rel}(\eta) \cdot C_\mathrm{abs}(p_\mathrm{T}') \cdot C_\mathrm{res}(p_\mathrm{T}'', \eta) \cdot p_\mathrm{T}^\mathrm{raw}, \tag{1.5}$$

398 where $p_\mathrm{T}^\mathrm{cor}$ is the corrected jet p_T and $p_\mathrm{T}^\mathrm{raw}$ is the fully uncorrected jet p_T. By the application
399 of the various correction factors, the jet transverse momentum is calibrated in a factorised
400 manner.

401 Throughout this thesis, all jets are calibrated by the application of the jet transverse
402 momentum correction factors, referred to as jet energy corrections.

Charged hadron subtraction

404 Particles originating from pileup vertices (additional vertices during a bunch crossing)
405 can be clustered into jets leading to higher energies of the reconstructed jet. Therefore a
406 procedure called charged hadron subtraction (CHS) is applied. It removes reconstructed
407 charged particles that do not originate from the primary vertex (see [38] for more details).

408 In this thesis, all jets are subject to charged hadron subtraction.

1.3.2.3 Reconstruction of muons

410 There are three different muon definitions at CMS [39]: global muons, tracker muons,
411 and standalone muons. They have all in common that they require energy deposits in
412 the muon system. The reconstruction of each of the three muon types is explained in the
413 following.

414 **Standalone muons:** For the reconstruction of standalone muons, all reconstructed seg-
415 ments in the muon system are utilised. Similar to the track reconstruction in the
416 tracking system, Kalman filter techniques [30] are exploited to reconstruct muon tra-
417 jectories in the muon chambers. A compatibility to the interaction point is imposed
418 to reconstruct only muons produced at the LHC (no cosmic muons). Further details
419 about the reconstruction of standalone muons can be found in [14, 40]

Tracker muons: To reconstruct so-called tracker muons, all tracker tracks with a $p_T >$ 0.5 GeV and $p > 2.5$ GeV are extrapolated to the muon system. If at least one muon segment is matched to a reconstructed track within certain quality criteria, the trajectory is considered as a tracker muon (see [39] for more detailed information).

Global muons: For the reconstruction of global muons an outside-in approach is utilised. For each reconstructed standalone muon, the compatibility to the reconstructed tracks in the tracking system is checked. If compatible, a global muon track is reconstructed using Kalman filter techniques. For high-p_T muons, the momentum resolution can be increased compared to the momentum estimated using tracker information only [39].

1.3.2.4 Reconstruction of electrons

The reconstruction of electrons at the CMS experiment is based on a mixture of the particle-flow algorithm explained in Section 1.3.1 and a standalone approach [41]. Thus, it is a very complex procedure and only the basic approach shall be reviewed here. The reader is referred to [42] for a complete description of the reconstruction procedure.

Electrons are identified using clustered energy deposits in the ECAL and reconstructed tracks in the tracker system. Both inputs are tested on compatibility and finally used to estimate the electron properties.

The difficulty of the electron reconstruction lies in the possibly large energy losses due to bremsstrahlung. This can change the direction of the electron significantly and lead to a reduced efficiency of the standard track reconstruction used for tracker tracks as well as a reduced efficiency of the association of ECAL clusters to the reconstructed track in the inner tracking system. Therefore, an optimised track reconstruction for electrons is additionally performed in order to account for direction changes due to the radiation of photons. Because the dedicated electron track reconstruction can be very time consuming, a seeding of tracker hits rely already on ECAL information to reduce the number of candidate tracks (ECAL-based seeding).

The electron reconstruction proceeds therefore as follows. First, ECAL clusters (so-called superclusters) are formed using a "hybrid" algorithm in the barrel region and "multi-5×5" algorithm in the endcaps. Due to bremsstrahlung, the energy deposits by electrons are usually spread out over several crystals. Additionally, so-called PF clusters are formed that add all contiguous crystals to the above mentioned superclusters. Afterwards, the standard track reconstruction is used to reconstruct electron tracks when bremsstrahlung is negligible. However, very short reconstructed tracks or tracks with a bad χ^2, are refitted using a so-called Gaussian sum filter (GSF) [43] to account for electrons with high radiative energy losses. As mentioned above, these tracks use ECAL-based seeding to reduce the number of candidate tracks. To identify these refitted tracks as candidate electron

tracks, a multivariate analysis is performed using tracker and ECAL information. For the GSF tracks, all ECAL PF clusters are added tangent to the electron track in order to add the energies from bremsstrahlung photons. Finally, track-cluster association criteria are applied in order to reduce misidentification when preserving a high reconstruction efficiency. The association criteria rely on spatial distances between the superclusters and the tracker track for ECAL-seeded tracks (GSF tracks) and rely on multivariate techniques for the tracker-seeded (standard track reconstruction) electrons.

1.3.2.5 Reconstruction of taus

The tau reconstruction at CMS refers to the reconstruction of hadronically decaying taus (a fraction of around 65% of taus decays hadronically). At CMS, the main algorithm used to identify and reconstruct taus is the so-called hadron plus strip algorithm (HPS) [44,45], which is also used in this thesis. The following description of the tau reconstruction algorithm follows [44].

The HPS algorithm performs in two separate steps. First, reconstructed PF particles are combined in a way that they are compatible with any of the tau decay modes and the four-momentum of this combined object is estimated. Second, multivariate techniques are used in order to discriminate the candidate taus against decays from gluon or quark jets and from muons and electrons. The HPS algorithm starts from reconstructed jets with a radius parameter of $R = 0.5$ and $p_\mathrm{T} > 14\,\mathrm{GeV}$ and $|\eta| < 2.5$.

The successful identification of a tau requires a reconstruction of a neutral pion which is present in most of the hadronic decays. Since a neutral pion decays into two photons in 99% which in turn convert into electron-pairs with a high probability, photon and electrons are clustered into strips in the $\eta - \phi$ plane in order to identify possible π^0. The initial position of the strip equals the position of the seed electron or photon (photon or electron with the highest p_T not yet clustered into any strip). The next-highest p_T electron/photon within a certain distance ($\eta \times \phi = 0.05 \times 0.20$) to the original strip is merged into the strip. Afterwards, the strip position is recalculated and the step is repeated. The clustering stops if no more electrons/photons are found.

After the reconstruction of the neutral pion, multiple decay modes hypothesis are tested by combining up to two clustered strips with one or three charged particles. For all hypothesis, several restriction on the invariant mass of the hadronically decaying tau are applied. Finally, the hypothesis fulfilling the invariant mass requirement and - in case this happens for more than one hypothesis - with a reconstructed tau with the highest p_T is chosen.

Furthermore, for all taus in this thesis, the discriminators which are used for the reduction of jet, electron and muon contamination are required to be less than zero (see [44] for further details on the discriminators).

Finally, a loose isolation criterion is demanded, which is calculated by the (pileup corrected) scalar sum of the transverse momentum of all charged particles and photons with a p_T larger than $0.5\,\mathrm{GeV}$ in a cone of $R = 0.5$ around the tau.

1.3.2.6 Reconstruction of missing transverse energy

The particle-flow missing transverse energy, PF $\not{E}_\mathrm{T}$, in an event is defined as the negative vectorial sum of all particle-flow particles. Thus - neglecting momentum mismeasurements- it refers to the transverse momentum of all invisible particles in the event. In order to avoid negative effects from e. g. tracker inefficiencies, non-linear calorimeter responses, etc., $\not{E}_\mathrm{T}$ can be more precisely measured by correcting the transverse momentum of all jets contained in an event with the jet energy corrections (see Section 1.3.2.2).

For a more detailed explanation of $\not{E}_\mathrm{T}$ as well as for information of the performance of the reconstruction, the reader is referred to [46]

1.3.3 Event cleaning

The two analysis described in this thesis are subject to an event cleaning procedure. It refers to the application of several filters to remove events with detector signals not caused by particles from the hard interaction. In the following, the filters are listed and a short description will be given.

HBHE noise filter: This filter rejects anomalous HCAL noise in the barrel (HB) and in the endcap (HE). The noise in the HCAL is mainly related to the hybrid photodiodes (HPD) and readout boxes (RBX). It rejects events considering pulse shape and hit multiplicity information into account.

CSC beam halo filter: Particles contained in the beam halo can induce signals in the detector. Therefore, events with a muon moving parallel to the beam are rejected.

HCAL laser event filter: This filter provides a list of events, where the laser used for the HCAL calibration fired when a bunch crossing occurred. Detector signals from the laser can be misinterpreted as particle signals and therefore, these events are removed.

ECAL dead cell filter: Events in which jets point towards a non-working ECAL cell are rejected. This filter relies on information of the surrounding crystals as well as on "trigger-primitive" information.

EE bad supercrystal filter: In the ECAL endcap, two supercrystals were not working properly. Therefore, events where at least one of the two crystals detected unnatural high energy deposits were removed.

Tracking failure filter: Sometimes, unnatural high energy deposits are recorded in the calorimeters without corresponding tracks in the inner tracking system. The reconstruction of tracks can fail, because of too many tracker seeds or because the hard interaction was too far away from the interaction point. This filter rejects therefore events, where less than 10% of the energy in the event was measured by the tracker.

Scraping filter (data only): When there are at least ten tracks in the event, at least 25% of them need to be flagged as high-purity tracks as defined in [47].

Tracking POG filter: Events with aborted track reconstruction and/or strip tracker noise are rejected.

1.4 Simulation of events

A very important input for physics analyses at particle colliders, is the use of simulated *pp*-collision events. They serve as comparison to measured data and can give an estimation of the expected number of background events for a given selection. Furthermore, they are used to study event kinematics for Standard Model and beyond-SM processes.

The generation of simulated samples is done with the help of Monte Carlo (MC) methods (see e. g. [48]). Monte Carlo techniques are used to randomly sample points according to a specified probability distribution. The underlying probability distributions for the event generation are the transition probabilities from the initial into all possible final states.

Besides the simulation of the hard interaction of the event, also the subsequent showering and hadronisation as well as the detector response needs to be simulated. In the following sections, a short introduction into the various steps of event simulation is given (see e.g. [49] for a more thorough introduction).

The first step of the event generation of *pp*-collision events consists of the simulation of the hard process, i. e. the primary interaction of two partons of the two colliding protons. Which type of partons are involved in the primary interaction is specified by the so-called parton distribution functions (PDFs). They describe the probability of a parton (up-, down-quarks, gluons, sea quarks) to carry a certain energy fraction of the proton energy and thus define the probability for each parton taking part at the hard interaction process. In this thesis, all simulated samples make use of the PDFs provided by the CTEQ group [50] FIXME: Check this.

Afterwards, the generation of the matrix element as well as the simulation of showering and hadronisation is performed. Throughout this thesis, the matrix element generator MADGRAPH [51] plus the event generator PYTHIA [52] or the event generator PYTHIA only are used. Since MADGRAPH only provides the generation of matrix elements, the subsequent showering and hadronisation is done by PYTHIA. For this task, particles produced in the hard interaction are matched to the particles produced in the showers in order to avoid a double-counting of emissions in multijet processes. Since MADGRAPH is responsible for the simulation of well separated partons whereas PYTHIA is suppose to simulate the soft and collinear showers, the event is rejected if the simulated shower - clustered with the k_T method (see Section 1.3.2.2) - has a too large radius parameter (MLM matching scheme [53]).

The formation of colour neutral particles, called hadronisation, and the subsequent decay of unstable particles is simulated with PYTHIA for all samples used in this thesis. A visualisation of the various steps performed for the generation of events is shown in Fig. 1.12.

In order to account for signals caused by the interaction of the non-primary partons of the interacting protons - called the underlying event (UE) - various models (tunes) are exploited. They rely on the measured signals in data in proton collisions without any hard interaction. Detector signals caused by additional interactions (pileup interactions)
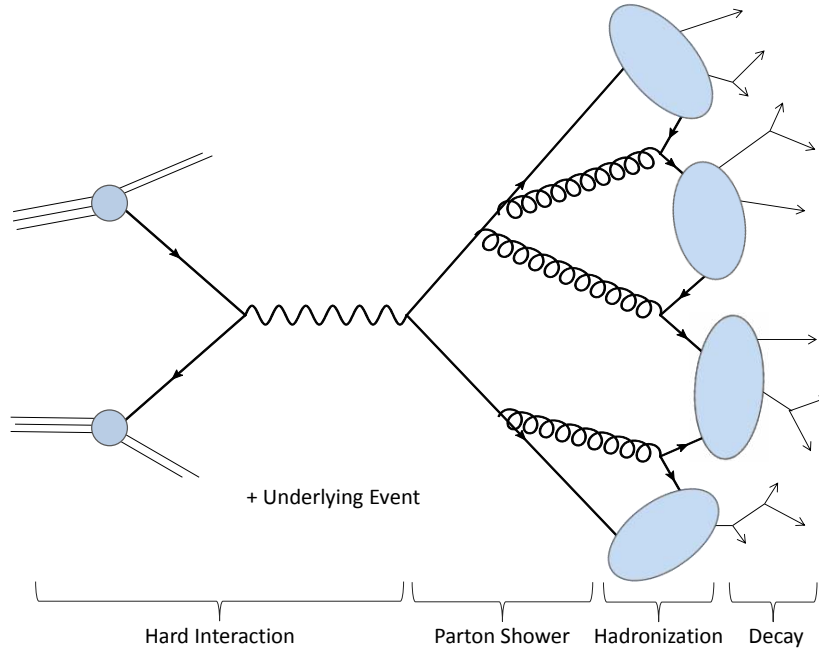

Figure 1.12: Visualisation of the various steps performed in the simulation of events. Taken from [36].

578 during a bunch-crossing, are also mixed into every simulated sample.

579 Finally, the interaction of the traversing particles with the detector material is simulated

580 with GEANT4 [54, 55] throughout this thesis.

Bibliography

[1] L. Evans and P. Bryant, "LHC Machine", *JINST* **3** (2008) S08001.
`doi:10.1088/1748-0221/3/08/S08001`.

[2] O. S. Bruning, P. Collier, P. Lebrun et al., "LHC Design Report Vol.1: The LHC
Main Ring", *Technical Design Report* **CERN-2004-003** (2004).

[3] "LEP Design Report: Vol.2. The LEP Main Ring",.

[4] CERN, "CERN, public web page". `www.cern.ch`. Accessed: 2016-01-17.

[5] CERN, "LHC: the guide", *CERN Brochure* **CERN-Brochure-2009-003-Eng**
(2009).

[6] CMS Collaboration, "The CMS experiment at the CERN LHC", *JINST* **3** (2008)
S08004. `doi:10.1088/1748-0221/3/08/S08004`.

[7] CMS Collaboration, "CMS physics: Technical design report", *Technical Design
Report* **CERN-LHCC-2006-001, CMS-TDR-008-1** (2006).

[8] ATLAS Collaboration, "The ATLAS Experiment at the CERN Large Hadron
Collider", *JINST* **3** (2008) S08003. `doi:10.1088/1748-0221/3/08/S08003`.

[9] ATLAS Collaboration, "ATLAS: Detector and physics performance technical design
report. Volume 1", *Technical Design Report*
CERN-LHCC-99-14,ATLAS-TDR-14 (1999).

[10] ATLAS Collaboration, "ATLAS: Detector and physics performance technical design
report. Volume 2", *Technical Design Report* **CERN-LHCC-99-15,
ATLAS-TDR-15** (1999).

[11] LHCb Collaboration, "The LHCb Detector at the LHC", *JINST* **3** (2008) S08005.
`doi:10.1088/1748-0221/3/08/S08005`.

[12] ALICE Collaboration, "The ALICE experiment at the CERN LHC", *JINST* **3**
(2008) S08002. `doi:10.1088/1748-0221/3/08/S08002`.

[13] CMS Collaboration, "CMS Luminosity - Public Results", *Public CMS Wiki* (2015).
https://twiki.cern.ch/twiki/bin/view/CMSPublic/LumiPublicResults, Topic
revision: r111.

[14] CMS Collaboration, "CMS Physics: Technical Design Report Volume 1: Detector Performance and Software", *Technical Design Report* **CERN-LHCC-2006-001,CMS-TDR-8-1** (2006).

[15] CMS Collaboration, "The CMS tracker system project: Technical Design Report", *Technical Design Report* **CERN-LHCC-98-006,CMS-TDR-5** (1997).

[16] CMS Collaboration, "The CMS tracker : addendum to the Technical Design Report", *Technical Design Report* **CERN-LHCC-2000-016** (2000).

[17] CMS Collaboration, "Description and performance of track and primary-vertex reconstruction with the CMS tracker", *JINST* **9** (2014), no. 10, P10009, `arXiv:1405.6569`. `doi:10.1088/1748-0221/9/10/P10009`.

[18] J. A. Sibille, "Radiation Hard Hybrid Pixel Detectors, and a bbbar Cross Section Measurement at the CMS Experiment". PhD thesis, Hamburg University, 2013. `http://cds.cern.ch/record/1569832`.

[19] CMS Collaboration, "Offline calibrations and performance of the CMS pixel detector", *Nucl. Instrum. Meth.* **A650** (2011) 25–29. `doi:10.1016/j.nima.2010.11.188`.

[20] CMS Collaboration, "Pixel Performance plots for 2012 data and simulation", *Public CMS Wiki.* https://twiki.cern.ch/twiki/bin/view/CMSPublic/PixelOfflinePlots2013, Topic revision: r22.

[21] CMS Collaboration, "The CMS electromagnetic calorimeter project: Technical Design Report", *Technical Design Report* **CERN-LHCC-97-033,CMS-TDR-4** (1997).

[22] CMS Collaboration, "The CMS hadron calorimeter project: Technical Design Report", *Technical Design Report* **CERN-LHCC-97-031,CMS-TDR-2** (1997).

[23] CMS Collaboration, "Performance of CMS Hadron Calorimeter Timing and Synchronization using Test Beam, Cosmic Ray, and LHC Beam Data", *JINST* **5** (2010) T03013, `arXiv:0911.4877`. `doi:10.1088/1748-0221/5/03/T03013`.

[24] CMS Collaboration, "The CMS muon project: Technical Design Report", *Technical Design Report* **CERN-LHCC-97-032,CMS-TDR-3** (1997).

[25] CMS Collaboration, "Particle-Flow Event Reconstruction in CMS and Performance for Jets, Taus, and MET", *CMS Physics Analysis Summary* **CMS-PAS-PFT-09-001** (2009).

[26] J. Nielsen, "Fundamentals of LHC Experiments", in *Proceedings, Theoretical Advanced Study Institute in Elementary Particle Physics (TASI 2010). String Theory and Its Applications: From meV to the Planck Scale*, pp. 127–152. 2011. `arXiv:1106.2516`.

[27] P. Billoir, "Progressive track recognition with a Kalman like fitting procedure", *Comput. Phys. Commun.* **57** (1989) 390–394. `doi:10.1016/0010-4655(89)90249-X`.

[28] P. Billoir and S. Qian, "Simultaneous pattern recognition and track fitting by the Kalman filtering method", *Nucl. Instrum. Meth.* **A294** (1990) 219–228. `doi:10.1016/0168-9002(90)91835-Y`.

[29] R. Mankel, "A Concurrent track evolution algorithm for pattern recognition in the HERA-B main tracking system", *Nucl. Instrum. Meth.* **A395** (1997) 169–184. `doi:10.1016/S0168-9002(97)00705-5`.

[30] R. Fruhwirth, "Application of Kalman filtering to track and vertex fitting", *Nucl. Instrum. Meth.* **A262** (1987) 444–450. `doi:10.1016/0168-9002(87)90887-4`.

[31] M. Cacciari, G. P. Salam, and G. Soyez, "The anti-k_t jet clustering algorithm", *JHEP* **04** (2008) 063, `arXiv:0802.1189`. `doi:10.1088/1126-6708/2008/04/063`.

[32] Y. L. Dokshitzer, G. D. Leder, S. Moretti et al., "Better jet clustering algorithms", *JHEP* **08** (1997) 001, `arXiv:hep-ph/9707323`. `doi:10.1088/1126-6708/1997/08/001`.

[33] M. Wobisch and T. Wengler, "Hadronization corrections to jet cross-sections in deep inelastic scattering", in *Monte Carlo generators for HERA physics. Proceedings, Workshop, Hamburg, Germany, 1998-1999*. 1998. `arXiv:hep-ph/9907280`.

[34] S. Catani, Y. L. Dokshitzer, M. H. Seymour et al., "Longitudinally invariant K_t clustering algorithms for hadron hadron collisions", *Nucl. Phys.* **B406** (1993) 187–224. `doi:10.1016/0550-3213(93)90166-M`.

[35] S. D. Ellis and D. E. Soper, "Successive combination jet algorithm for hadron collisions", *Phys. Rev.* **D48** (1993) 3160–3166, `arXiv:hep-ph/9305266`. `doi:10.1103/PhysRevD.48.3160`.

[36] K. Goebel, "Probing supersymmetry based on precise jet measurements at the CMS experiment". PhD thesis, Hamburg University, 2015. `http://www-library.desy.de/cgi-bin/showprep.pl?thesis15-003`.

[37] CMS Collaboration, "Determination of jet energy calibration and transverse momentum resolution in CMS", *JINST* **6** (2011) P11002, `arXiv:1107.4277`. `doi:10.1088/1748-0221/6/11/P11002`.

[38] CMS Collaboration, "Pileup measurement and mitigation techniques in CMS", *J. Phys. Conf. Ser.* **404** (2012) 012045. `doi:10.1088/1742-6596/404/1/012045`.

[39] CMS Collaboration, "Performance of CMS muon reconstruction in pp collision events at $\sqrt{s} = 7$ TeV", *JINST* **7** (2012) P10002, `arXiv:1206.4071`. `doi:10.1088/1748-0221/7/10/P10002`.

[40] CMS Collaboration, "Performance of CMS Muon Reconstruction in Cosmic-Ray Events", *JINST* **5** (2010) T03022, `arXiv:0911.4994`. `doi:10.1088/1748-0221/5/03/T03022`.

[41] S. Baffioni, C. Charlot, F. Ferri et al., "Electron reconstruction in CMS", *Eur. Phys. J.* **C49** (2007) 1099–1116. `doi:10.1140/epjc/s10052-006-0175-5`.

[42] CMS Collaboration, "Performance of electron reconstruction and selection with the CMS detector in proton-proton collisions at $\sqrt{s} = 8\,\text{TeV}$", *JINST* **10** (2015), no. 06, P06005, `arXiv:1502.02701`. `doi:10.1088/1748-0221/10/06/P06005`.

[43] W. Adam, R. Fruhwirth, A. Strandlie et al., "Reconstruction of electrons with the Gaussian sum filter in the CMS tracker at LHC", *eConf* **C0303241** (2003) TULT009, `arXiv:physics/0306087`. [J. Phys.G31,N9(2005)]. `doi:10.1088/0954-3899/31/9/N01`.

[44] CMS Collaboration, "Reconstruction and identification of τ lepton decays to hadrons and ν_τ at CMS", *JINST* **11** (2016), no. 01, P01019, `arXiv:1510.07488`. `doi:10.1088/1748-0221/11/01/P01019`.

[45] CMS Collaboration, "Performance of tau-lepton reconstruction and identification in CMS", *JINST* **7** (2012) P01001, `arXiv:1109.6034`. `doi:10.1088/1748-0221/7/01/P01001`.

[46] CMS Collaboration, "Performance of the CMS missing transverse momentum reconstruction in pp data at $\sqrt{s} = 8$ TeV", *JINST* **10** (2015), no. 02, P02006, `arXiv:1411.0511`. `doi:10.1088/1748-0221/10/02/P02006`.

[47] CMS Collaboration, "Tracking and Vertexing Results from First Collisions", *CMS Physics Analysis Summary* **CMS-PAS-TRK-10-001** (2010).

[48] S. Weinzierl, "Introduction to Monte Carlo methods", `arXiv:hep-ph/0006269`.

[49] M. Schröder, "Quality of jet measurements and impact on a search for new physics at CMS". PhD thesis, Hamburg University, 2012.
`http://www-library.desy.de/cgi-bin/showprep.pl?thesis12-042`.

[50] J. Pumplin, D. R. Stump, J. Huston et al., "New generation of parton distributions with uncertainties from global QCD analysis", *JHEP* **07** (2002) 012, `arXiv:hep-ph/0201195`. `doi:10.1088/1126-6708/2002/07/012`.

[51] J. Alwall, R. Frederix, S. Frixione et al., "The automated computation of tree-level and next-to-leading order differential cross sections, and their matching to parton shower simulations", *JHEP* **07** (2014) 079, `arXiv:1405.0301`. `doi:10.1007/JHEP07(2014)079`.

[52] T. Sjostrand, S. Mrenna, and P. Z. Skands, "PYTHIA 6.4 Physics and Manual", *JHEP* **05** (2006) 026, `arXiv:hep-ph/0603175`. `doi:10.1088/1126-6708/2006/05/026`.

[53] M. L. Mangano, M. Moretti, F. Piccinini et al., "Matching matrix elements and shower evolution for top-quark production in hadronic collisions", *JHEP* **01** (2007) 013, `arXiv:hep-ph/0611129`. `doi:10.1088/1126-6708/2007/01/013`.

[54] GEANT4 Collaboration, "GEANT4: A Simulation toolkit", *Nucl. Instrum. Meth.* **A506** (2003) 250–303. `doi:10.1016/S0168-9002(03)01368-8`.

[55] J. Allison et al., "Geant4 developments and applications", *IEEE Trans. Nucl. Sci.* **53** (2006) 270. `doi:10.1109/TNS.2006.869826`.